Supporting Information

Dynamic photoelectrochemical device using electrolyte-permeable $NiO_x/SiO_2/Si$ photocathode with an open circuit potential of 0.75 V

Jin-Young Jung, Jin-Young Yu and Jung-Ho Lee*

Departments of Materials and Chemical Engineering, Hanyang University, 55 Hanyangdaehak-ro, Sangnok-gu, Ansan, Kyeonggi-do 426-791, Republic of Korea

*Corresponding author:

E-mail:jungho@hanyang.ac.kr

Hanyang University, Korea

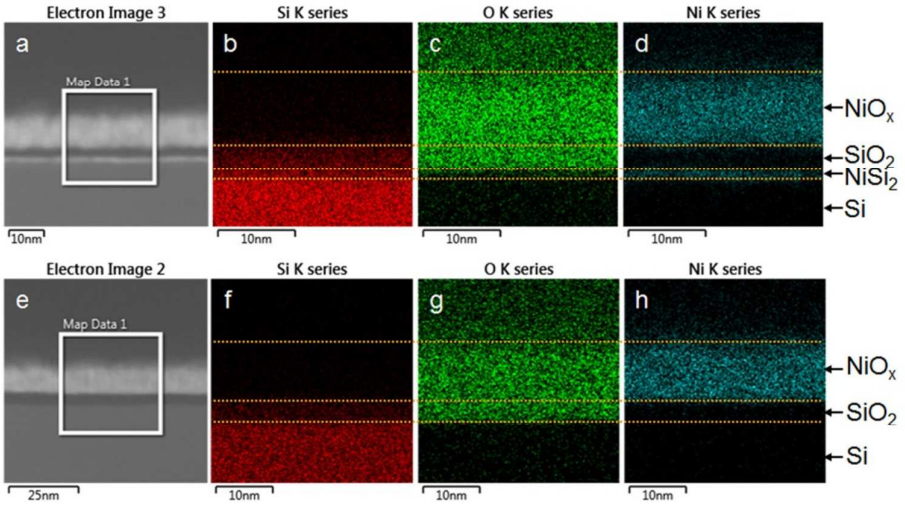

Figure S1. Results of elemental mapping determined using STEM with EDXS for NiO_x thin film coated onto (a–d) H-terminated Si and (e–h) SiO_2-grown Si.

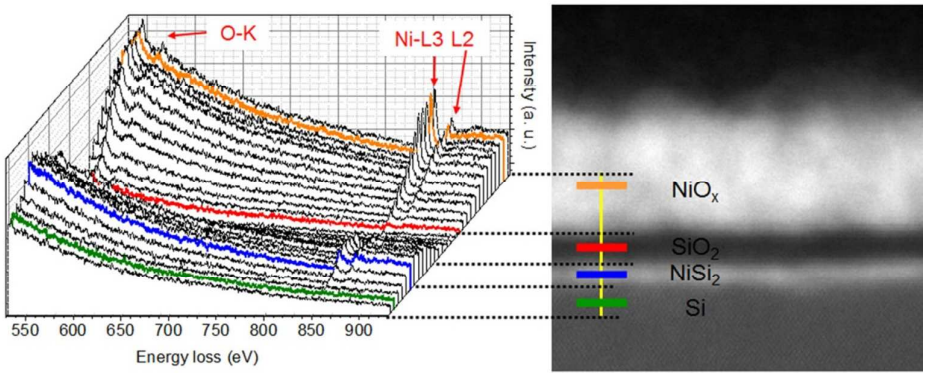

Figure S2. Elemental analysis of electron energy loss spectroscopy (EELS) in the interface layers of $NiO_x/SiO_2/NiSi_2/Si$. In the Ni-$L_{2,3}$ edge spectra of $NiSi_2$ layer, a branching ratio, defined as the ratio of the L_3 area to the sum of the L_2 and L_3 area, is calculated to be 0.755, indicating the $NiSi_2$ phase.

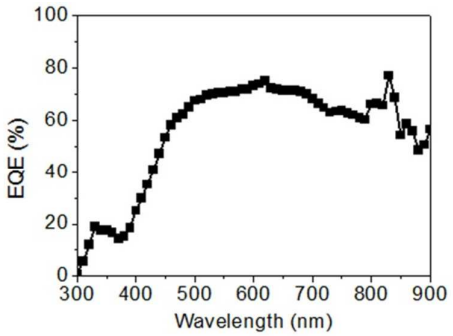

Figure S3. External quantum efficiency of $NiO_x/SiO_2/Si$ photocathode.

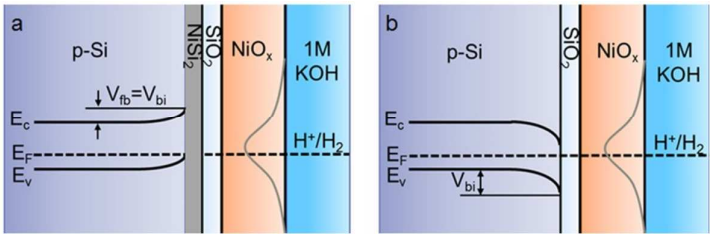

Figure S4. Schematic representation describing the approximate energy band diagrams for (a) NiO_x/Si and (b) $NiO_x/SiO_2/Si$ photocathodes, based upon the V_{bi} results shown in Fig. 1d.

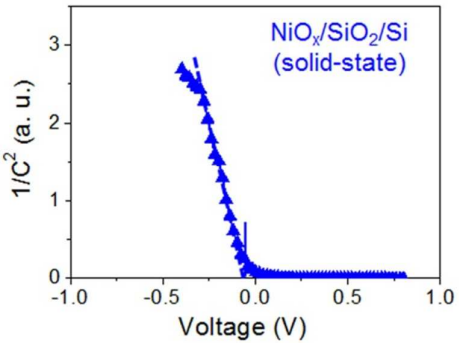

Figure S5. M–S plots obtained for the solid-state device fabricated using $NiO_x/SiO_2/Si$.

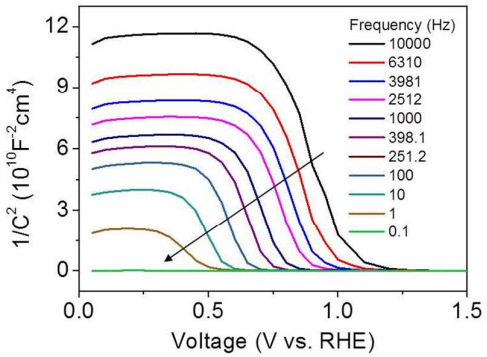

Figure S6. M–S plots obtained for the electrolyte/NiO_x/n^+-Si at various frequencies (0.1–10,000 Hz) to characterize the energetics of the NiO_x/electrolyte system. The changes in V_{fb} as a function of frequency show that the Fermi-level of NiO_x varies with the reduction rate.

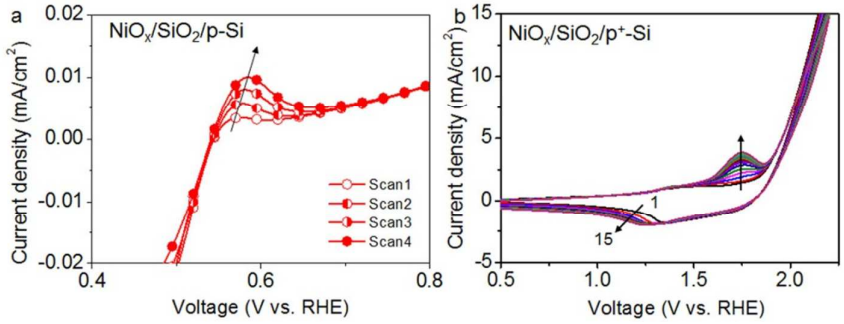

Figure S7. Reduced and oxidized NiO_x thin film. (a**)** Oxidation waves at anodic current region of illuminated LSV curve for NiO_x/SiO_2/Si photocathode. (b**)** Cyclic voltammograms for NiO_x/SiO_2/p^+-Si in 1 M KOH obtained over 15 cycles at a scan rate of 100 mV/s, indicating the reduction/oxidation of NiO_x. The growth and shift for the reduction and oxidation waves with the repetitive cycling of CV is attributed to the increase in the reduction area, i.e., indicating the reduction reaction occurring over the entire bulk and not just the surface as observed in previous works (see Refs. 30 and 40 in the references of main manuscript). Therefore, our NiO_x thin film can be regarded to possess an electrolyte-permeable, porous structure, which enables reduction to effectively change the Fermi-level of NiO_x.

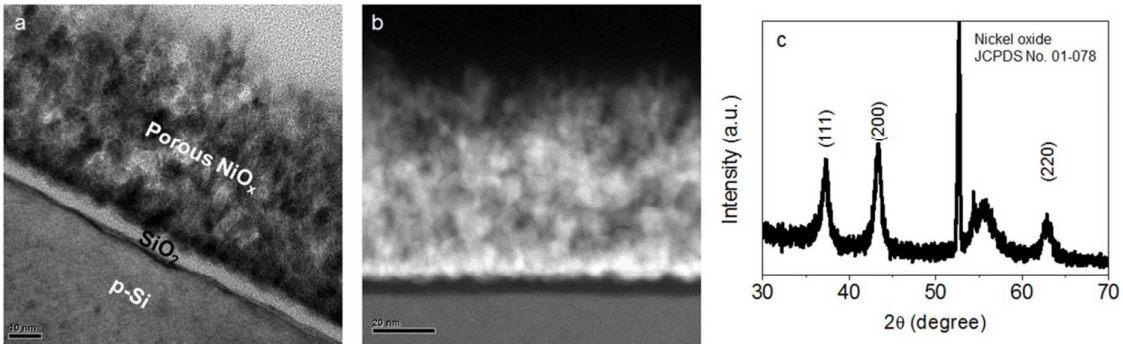

Figuer S8. (a) TEM image, (b**)** STEM image, and (c) X-ray diffraction (XRD) pattern of NiO_x thin film of a 40-nm-thin NiO_x film coating on a SiO_2-grown Si wafer, clearly showing the electrolyte-permeable, poly-crystalline structure of the NiO_x thin film with a small grain size in the range of 2 to 5 nm.

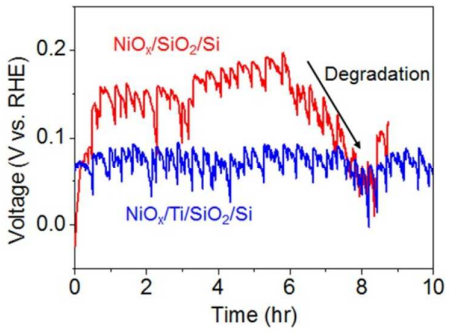

Figure S9. Chronopotentiometry results obtained for $NiO_x/SiO_2/Si$ photocathode (red) and $NiO_x/Ti/SiO_2/Si$ photocathode (blue) under illumination at a constant photocurrent of −10 mA/cm^2. The improved stability by Ti layer inserted between NiO_x and SiO_2 suggests that NiO_x thin film is electrolyte-permeable.

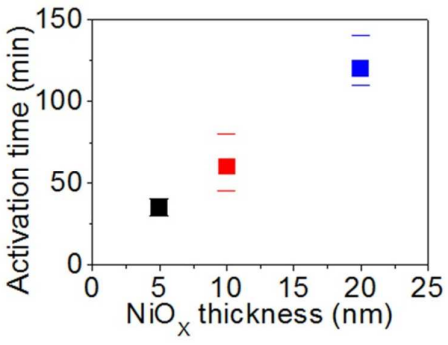

Figure S10. Plot showing NiO_x thickness dependent activation times required for the saturation of the HER potential level determined using CP measurements shown in Fig. 2b.

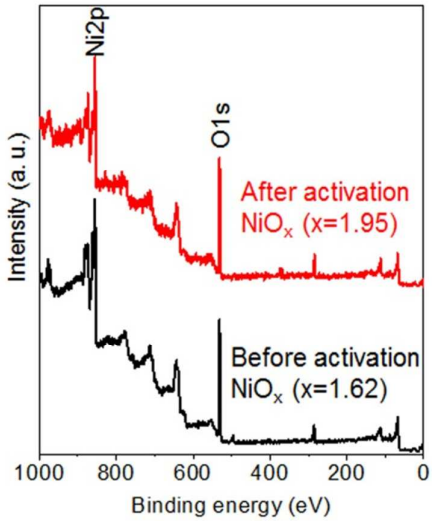

Figure S11. XPS survey spectra of NiO_x thin film before and after the activation process.

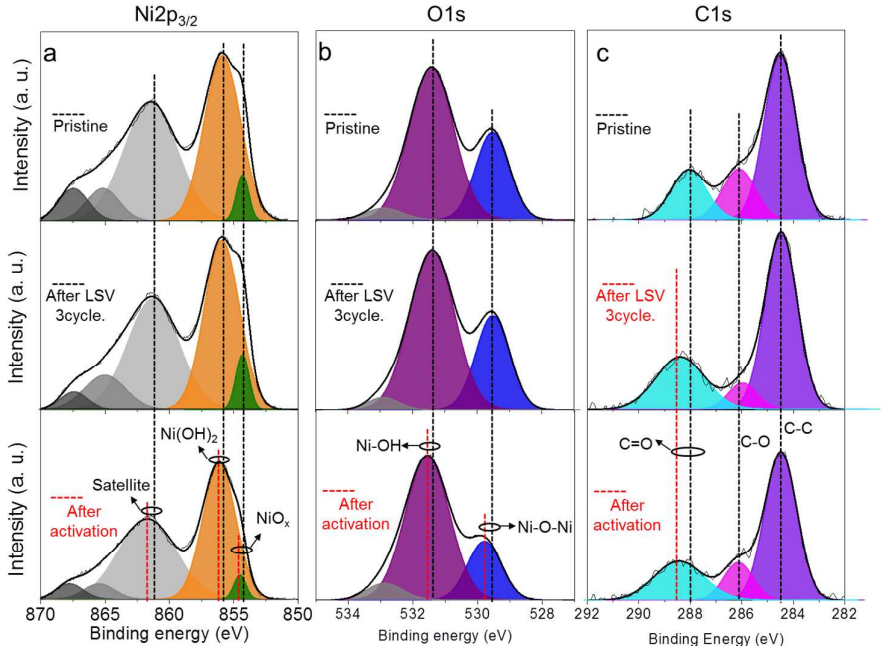

Figure S12. (a) Ni 2p, (b) O 1s, and (c) C 1s XPS spectra of the NiO_x thin film in pristine (top) and test samples after LSV response for 3 cycles (middle) and activation process (bottom). The obtained results revealed that the peak positions in Ni 2p and O 1s after LSV response for just 3 cycles were unchanged, while the peak positions were shifted for the activation sample. The results in C 1s spectra showed that C=O peak was broadened and shifted to a high-energy side for both the 3 cycle LSV and the activation samples, due to the carbon contamination during PEC reaction.

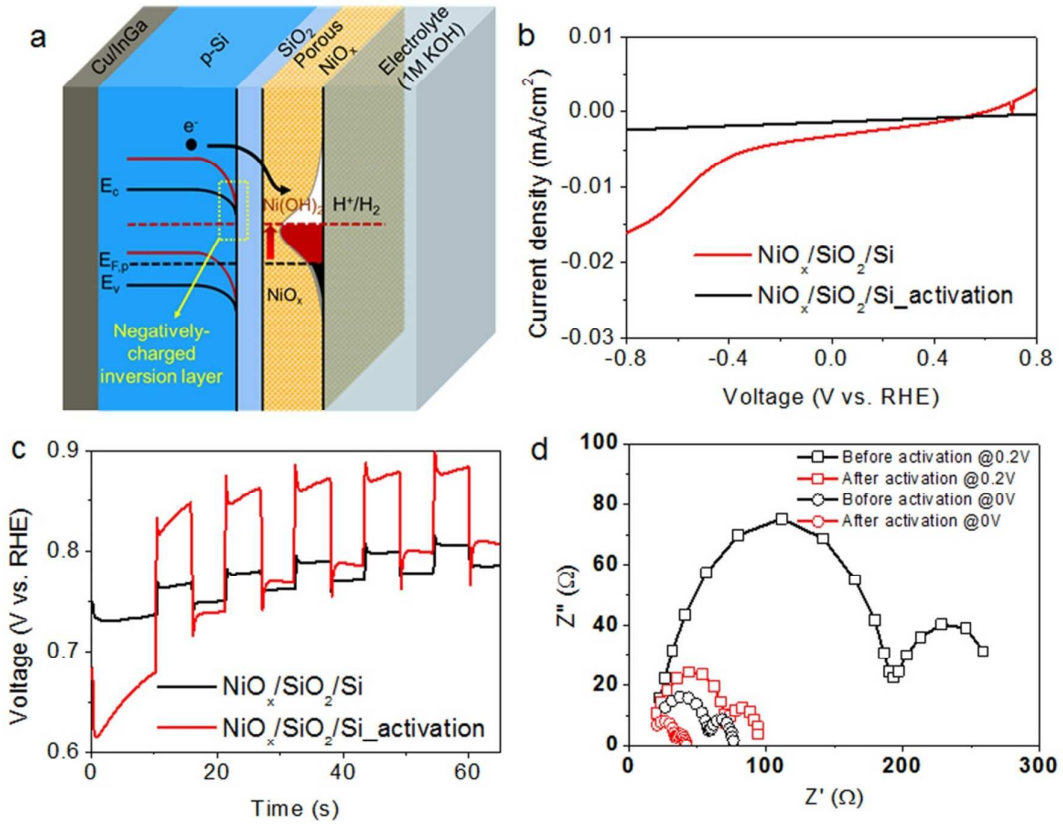

Figure S13. Effect of a large V_{bi} on PEC performances. (a**)** Schematic representation showing the structure and approximate energy band diagram of the electrolyte-permeable $NiO_x/SiO_2/Si$ photocathode with effective change of V_{bi} induced by the transformation of NiO_x into $Ni(OH)_2$ over the entire layer. Comparison of PEC performance parameters, including (b) dark (leakage) current, (c) photovoltage, and (d) charge transfer resistance as determined by electrochemical impedance spectroscopy (EIS) before (black) and after (red) the activation process. The decrease in the dark current signifies suppressed recombination loss, which causes an increase in photovoltage. The EIS results show a decrease in the hemisphere diameter after the activation process, thus indicating an improvement in charge transfer kinetics.

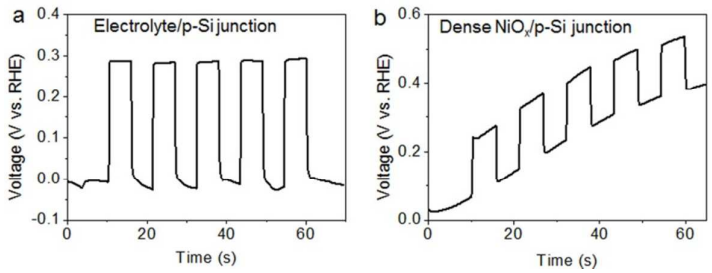

Figure S14. The V_{ph} results for (a) the electrolyte/p-Si junction and (b) the dense NiO_x/p-Si junction. The dense NiO_x was deposited by sputtering process.

In case of the nano-sized, porous structures, the mixed potential due to two partial reactions of NiO_x and KOH electrolyte can be also considered to affect an interfacial energetics of the Si photocathode. But, the mixed potential can be excluded from our study because they should generate a constant V_{ph}, as observed in an electrolyte/p-Si junction and an electrolyte-impermeable NiO_x/Si junction (Supplementary Fig. S14).

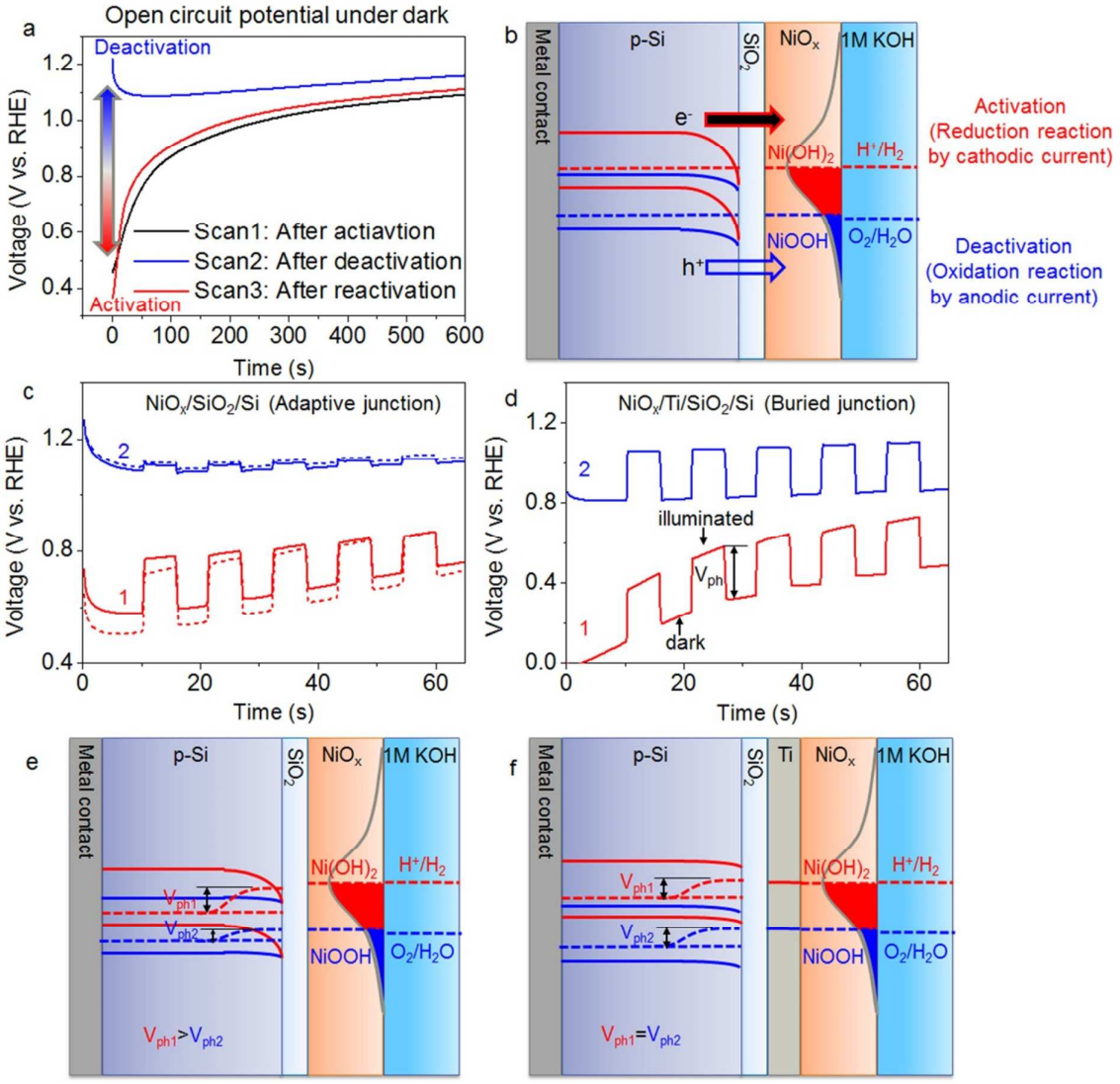

Figure S15. Change in V_{ph} for the adaptive junction. (a**)** Potential measurement of the $NiO_x/SiO_2/Si$ photocathode as a function of time under open circuit conditions in the dark after preconditions such as activation, deactivation, and reactivation. After the activation process performed by operation of the HER (reduction reaction), the open circuit potential under dark conditions ($OCP_{@dark}$) was found to be at the most cathodic potential level (see black curve). However, during the measurement, an anodic shift in the $OCP_{@dark}$ level was observed with increasing time due to deactivation, caused by tunneling of the majority of hole carriers (h^+) from Si into NiO_x (oxidation reaction). When the potential measurement was implemented just after deactivation, the $OCP_{@dark}$ remained at a potential level of ~1.2 V under dark conditions (see blue curve). After operating the HER again for reactivation (see red curve), the $OCP_{@dark}$ returned to the initial potential level of the black curve. (b) Schematic illustrations show the band diagram of the $NiO_x/SiO_2/Si$ photocathode under dark conditions in an equilibrium state just after activation and deactivation. (c–f) The V_{ph} measurements and schematic illustrations of the band diagram of the $NiO_x/SiO_2/Si$ photocathode (c, e) and $NiO_x/Ti/SiO_2/Si$

photocathode (d, f). The V_{ph} measurements were carried out in two consecutive runs. The V_{ph} for the $NiO_x/SiO_2/Si$ photocathode changed as a function of varying $OCP_{@dark}$, while that for the $NiO_x/Ti/SiO_2/Si$ photocathode remained unchanged.

As described in Supplementary Figs. S15(a) and (b), the changes in $OCP_{@dark}$ indicate that the Fermi level of NiO_x is altered according to the reduction reaction (activation) by the cathodic current and the oxidation reaction (deactivation) by the anodic current. After the HER (activation), the reduction level for $Ni(OH)_2$ was matched to the Fermi level of p-Si at the equilibrium state (see red lines in Supplementary Figs. S15(e) and (f)). Whereas the oxidation level for NiOOH was matched after the potential measurement under open circuit conditions in darkness (deactivation, see blue lines in Supplementary Figs. S15(e) and (f)). Consequently, the change in V_{ph} for the $NiO_x/SiO_2/Si$ photocathode with an anodic shift of the $OCP_{@dark}$ was evident for the adaptive NiO_x/Si junction (see Supplementary Figs. S15(c) and (e)). On the other hand, the unchanged V_{ph} for the $NiO_x/Ti/SiO_2/Si$ photocathode evidences the buried Ti/Si junction (see Figs. S15(d) and (f)).

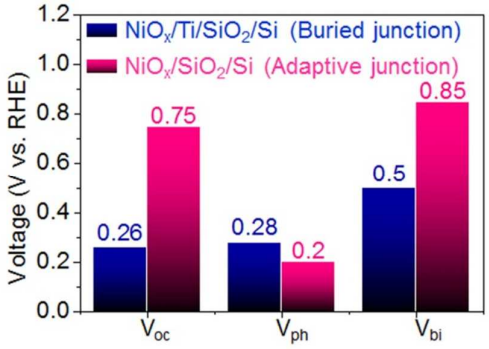

Figure S16. Comparison of PEC performance trends using parameters such as OCP, V_{ph}, and V_{bi} for $NiO_x/SiO_2/Si$ and $NiO_x/Ti/SiO_2/Si$ photocathodes.

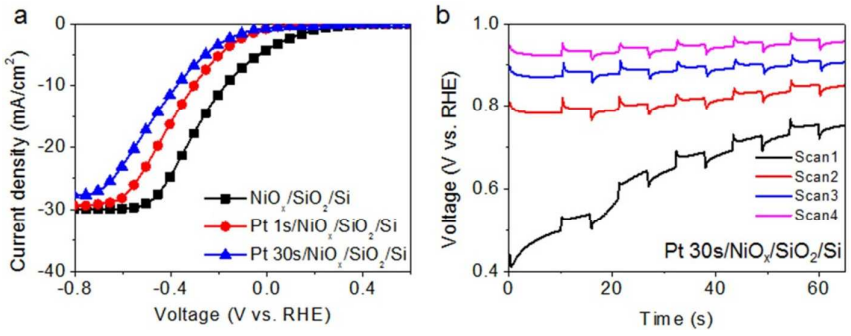

Figure S17. (a) LSV responses and (b) photovoltage measurements obtained for the Pt catalyst-coated $NiO_x/SiO_2/Si$ photocathode. The cathodic shift of the LSV curve and the fixed value of V_{ph}, indicate degradation in the PEC performance and the dissipation of the adaptive junction behavior, respectively.

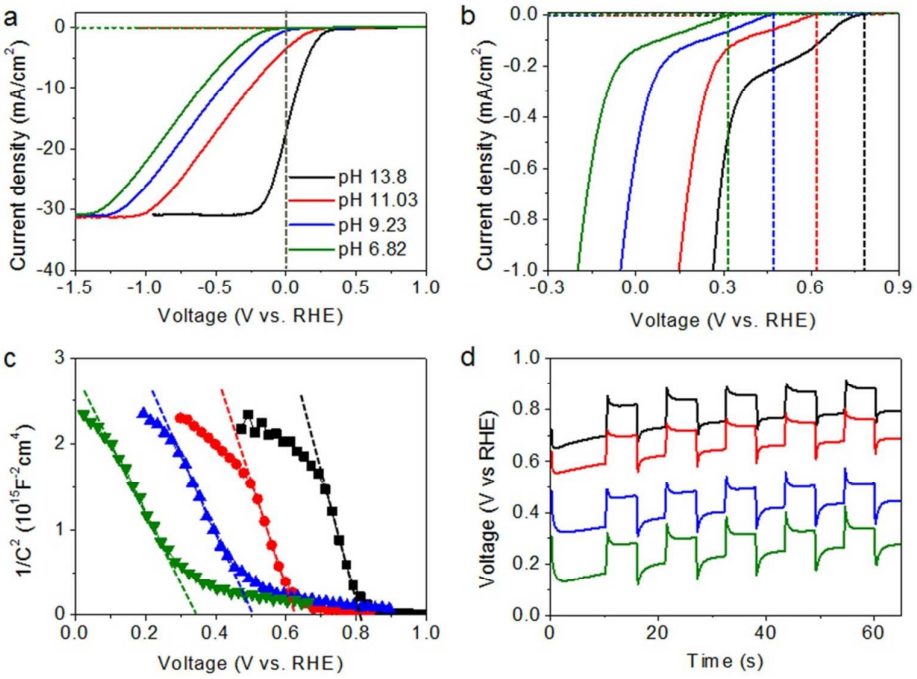

Figure S18. Redox potential (electrolyte pH) dependent OCP and V_{bi} (a, b) LSV responses, (c) M–S plots, and (d) photovoltage measurements obtained for the $NiO_x/SiO_2/Si$ photocathode at different electrolyte pH levels (6.8–13.8). The vertical dot lines denote the OCPs. The changes in both V_{fb} and OCP as a function of electrolyte pH indicate that the redox potential level contributed to the interfacial energetics of the adaptive NiO_x/Si junction. By contrast, the maximum V_{ph} remained nearly unchanged, suggesting that OCP is independent of V_{ph}.

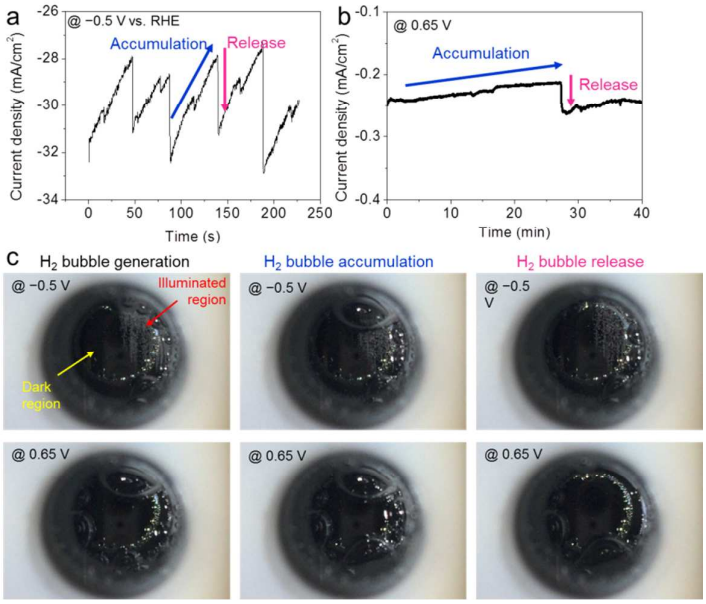

Figure S19. Chronoamperometry measurements of $NiO_x/SiO_2/Si$ photocathode at applied (a) −0.5 V (vs RHE) generating a limited current of ~32 mA/cm^2 and (b) 0.65 V (vs. RHE) close to the 0.75 V OCP. (c) Digital photos showing the representative conditions of H_2 bubbles.

The chronoamperometry curves of the Si photocathode (Figure S19a and b) and digital photos reflecting some status of hydrogen bubbles in the chronoamperometry (Figure S19c) exhibited the H_2 bubble generation, accumulation, and release during PEC reactions. Applying −0.5 V vs. RHE generating a limited current of ~32 mA/cm^2 generated a large amount of H_2 bubbles only at the illuminated region (see top left image), and the generated H_2 bubble was accumulated at the edge of samples (top middle) and finally released when no longer sustained for accumulation (top right). More specifically, the current density level gradually declined when bubbles accumulated; then restores its original current level at the release of bubbles. Applying 0.65 V close to the OCP, accumulation and release of bubbles still happened even though bubble generation was not clearly observed, displaying the OCP resulted from the Faradaic reaction of H_2 evolution.

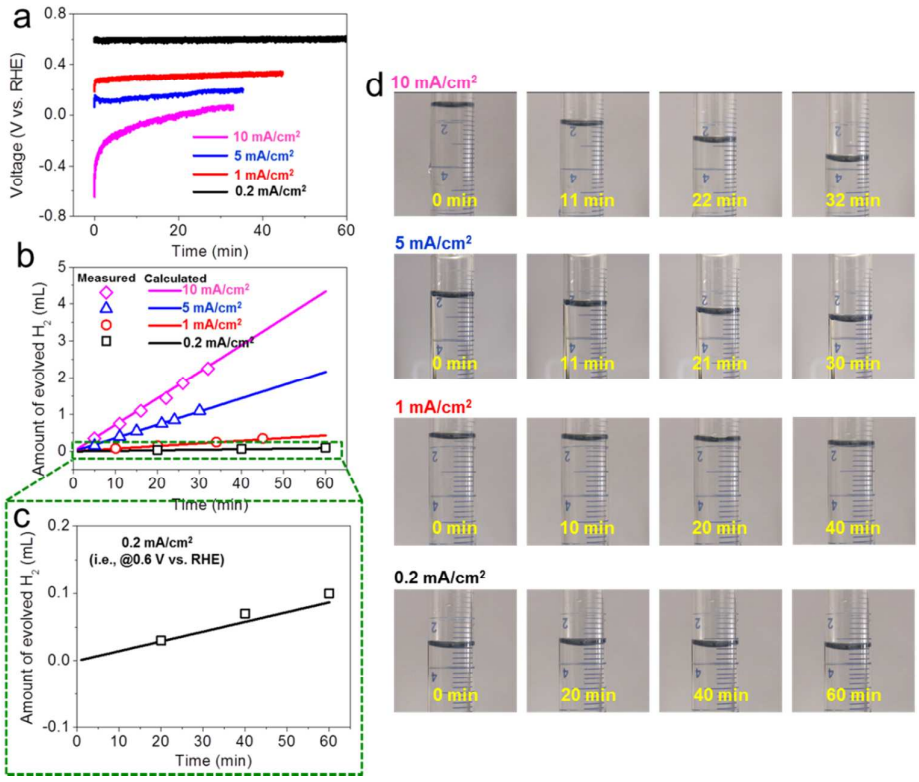

Figure S20. Hydrogen evolution measured by volume displacement. (a) Chronopotentiometry measurements of $NiO_x/SiO_2/Si$ photocathode with varying the current levels from 0.2 to 10 mA/cm^2. (b, c) Plots showing an amount of the H_2 evolved under the chronopotentiometry measurements of (a). Symbols (measured) and solid lines (calculated) denote the volumes of collected hydrogen. The panel (c) represents a low volume level range (<0.2 mL) of the panel (b). (d) Digital photos showing the volume changes corresponding to the measured results of panel (b). The volume changes were observed by the water menisci inside a graduated flask suppressed due to H_2 evolution from the top-side of the flask.

We have measured the amount of H_2 evolved during chronopotentiometry operation at varying the current levels from 0.2 to 10 mA/cm^2, as shown in Figure S20. The volume change observed at the low current level of 0.2 mA/cm^2 close to the OCP means that the H_2 evolution occurs even in the OCP. In addition, the measured H_2 volumes were estimated to be closely matched to the calculated values from the Faraday's law of electrolysis, indicating a 100% Faraday efficiency.

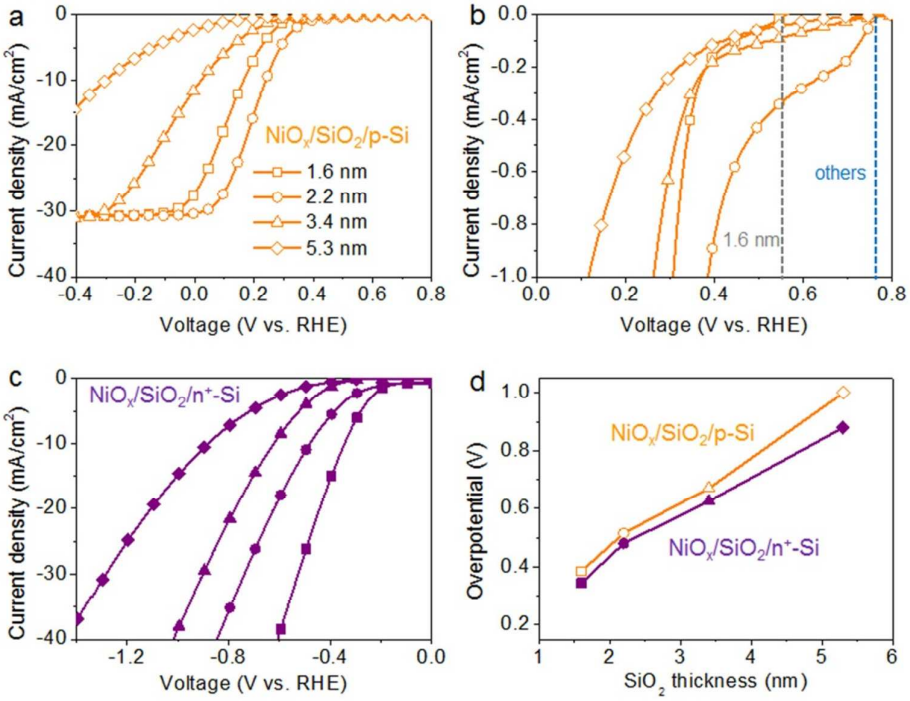

Figure S21. Increased charge transfer resistance with SiO_2 thickness. (a, b) Illuminated LSV responses of the NiO_x/SiO_2/p-Si samples with varying SiO_2 thickness. The plot in (b) represents the low photocurrent density level range (<−1 mA/cm^2) of the plot shown in (a), and used to identify the OCP. (c) dark LSV responses of the $NiO_x/SiO_2/n^+$-Si samples. (d**)** Plots showing overpotentials of both the p-Si and the n^+-Si samples with SiO_2 thickness.